IOP Publishing Journal of Physics: Condensed Matter
J. Phys.: Condens. Matter **0** (2021) 000000 (11pp) https://doi.org/10.1088/1361-648X/abd781

Magnetoelastic coupling and spin contributions to entropy and thermal transport in biferroic yttrium orthochromite

Naini Bajaj[1], Aditya Prasad Roy[1], Ashish Khandelwal[2], M K Chattopadhyay[2,3], Vasant Sathe[4], Sanjay K Mishra[5], Ranjan Mittal[5], Peram Delli Babu[5], Manh Duc Le[6], J L Niedziela[7] and Dipanshu Bansal[1]

[1] Indian Institute of Technology Bombay, Mumbai, MH 400076, India
[2] Free Electron Laser Utilization Laboratory, Raja Ramanna Centre for Advanced Technology, Indore, MP 452013, India
[3] Homi Bhabha National Institute, Training School Complex, Anushakti Nagar, Mumbai, MH 400094, India
[4] UGC-DAE Consortium for Scientific Research, University Campus, Khandwa Road, Indore, MP 452001, India
[5] Solid State Physics Division, Bhabha Atomic Research Centre, Mumbai, MH 400085, India
[6] ISIS facility, Rutherford Appleton Laboratory, Chilton, Didcot, OX11 0QX, Oxfordshire, United Kingdom
[7] Nuclear Nonproliferation Division, Oak Ridge National Laboratory, Oak Ridge, TN 37831, United States of America

E-mail: niedzielajl@ornl.gov and dipanshu@iitb.ac.in

Received 28 October 2020, revised 3 December 2020
Accepted for publication 18 December 2020
Published XX XX XXXX

Abstract

Direct engineering of material properties through exploitation of spin, phonon, and charge-coupled degrees of freedom is an active area of development in materials science. However, the relative contribution of the competing orders to controlling the desired behavior is challenging to decipher. In particular, the independent role of phonons, magnons, and electrons, quasiparticle coupling, and relative contributions to the phase transition free energy largely remain unexplored, especially for magnetic phase transitions. Here, we study the lattice and magnetic dynamics of biferroic yttrium orthochromite using Raman, infrared, and inelastic neutron spectroscopy techniques, supporting our experimental results with first-principles lattice dynamics and spin-wave simulations across the antiferromagnetic transition at $T_N \sim 138$ K. Spectroscopy data and simulations together with the heat capacity (C_p) measurements, allow us to quantify individual entropic contributions from phonons ($0.01 \pm 0.01 k_B$ atom^{-1}), dilational ($0.03 \pm 0.01 k_B$ atom^{-1}), and magnons ($0.11 \pm 0.01 k_B$ atom^{-1}) across T_N. High-resolution phonon measurements conducted in a magnetic field show that anomalous T-dependence of phonon energies across T_N originates from magnetoelastic coupling. Phonon scattering is primarily governed by the phonon–phonon coupling, with little contribution from magnon–phonon coupling, short-range

* Author to whom any correspondence should be addressed.

spin correlations, or magnetostriction effects; a conclusion further supported by our thermal conductivity measurements conducted up to 14 T, and phenomenological modeling.

Keywords: magnetoelastic coupling, thermal conductivity, thermodynamics, neutron scattering, density functional theory, magnetoelectrics, multiferroics

S Supplementary material for this article is available online

Q5 (Some figures may appear in colour only in the online journal)

1. Introduction

The interplay of spin, phonon, and electronic degrees of freedom (DoF) induces fascinating material properties such as unconventional superconductivity [1, 2], the metal–insulator transition [3], and multiferroicity [4]. While this interplay allows for tunable properties with control parameters, i.e., temperature, pressure, carrier concentration, and magnetic field, it also brings along a web of complexity to untangle. In particular, it is difficult in complex systems to pinpoint the DoF essential to driving material properties, particularly in cases exhibiting coupling between different DoF. Detailed knowledge of phonons, spin waves (magnons), and electronic structure combined with thermodynamic analysis (i.e., entropy) across a thermodynamic transition can unambiguously clarify these aspects. For instance, mapping phonons, magnons, and the electronic structure across the Brillouin zone using inelastic neutron/x-ray experiments and simulations has been critical to identify the entropy component of the first-order structural phase transition occurring concurrently with metal–insulator transition in VO_2 [5] and h-FeS [6].

Biferroics (or multiferroics) host spontaneous and switchable ferroelectric (FE) polarization P and magnetization M. As they are generally wide-gap semiconductors or insulators, the electronic coupling effects can be eliminated and investigation of these systems offers an opportunity to unravel coupling between spin and phonon DoF across the antiferromagnetic (AFM) phase transition [4, 7].

In type-I multiferroics, P is governed by phonon eigenvectors that are frozen into the lattice below the FE transition temperature, T_{FE}, resulting in a structural distortion that breaks the inversion symmetry. Consequently, temperature-dependent phonon measurements are necessary to rationalize the origin of P across T_{FE} [8, 9]. On further cooling to the biferroic phase, i.e., $T < T_N$ and $T < T_{FE}$, phonons show anomalous T-dependence resultant from magnetoelastic and magnon–phonon coupling. In magnetoelastic coupling, magnetic ordering below T_N shifts the average atomic positions [10, 11], and consequently modifies the interatomic force constants and T-dependence of phonons [12]. However, in the magnon–phonon coupling, phonons directly couple to magnons via hybridization of the two (i.e., electromagnons [13–15]) or via coupled spin-lattice Hamiltonian and magnon–phonon scattering channels [16]. Application of B further modifies the phonon response via a change to the lattice Hamiltonian [17, 18], or via magnetoelastic and magnetostriction (lattice strains due to applied B) effects [11]. Given that several mechanisms could control the phonon response and resultant P in the biferroic phase, delineation of the role of phonons and magnons is necessary to gain a comprehensive understanding of how to control of biferroics/multiferroics for technological applications.

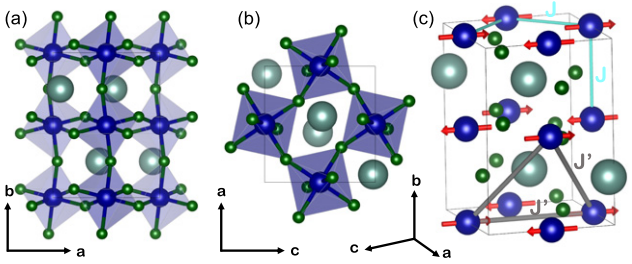

Figure 1. (a), (b) Crystal structure of $YCrO_3$ showing CrO_6 polyhedron and their tilts. Y, Cr, and O are denoted by light green, blue, and green colors, respectively. (c) Same as panel (a) but showing the direction of magnetic moments (red color arrows) and exchange interactions J (cyan lines) and J' (gray lines) between different Cr pairs used to model the spin waves.

Yttrium orthochromite ($YCrO_3$), because of its biferroic properties [19], and extensive characterization using physical/magnetic property measurements [19–25], is an ideal system to delineate the role of phonons and magnons. $YCrO_3$ undergoes a FE transition at $T_{FE} \sim 473$ K with $P \sim 2\ \mu C\ cm^{-2}$ at 300 K [19], comparable to $P \sim 5\ \mu C\ cm^{-2}$ of the archetypal geometric improper FE $YMnO_3$ at 300 K [26]. Cooling below $T_N \sim 140$ K, G-type AFM order sets in with spins pointing along the c-axis [27] (see figure 1). While the static lattice and magnetic structure/properties of $YCrO_3$ are well understood, little is known about the thermodynamic and spectroscopic behavior. Heat capacity (C_p) data [21, 23] suggests a spin-orientation transition, but there is no experimental evidence in magnetization measurements [22]. Phonon energies (ω) are reported to have an anomalous T-dependence (decrease in ω on cooling) for certain modes [28–30], however the source of such anomalies remains unclear. Furthermore, while the low thermal conductivity (κ) of $Y_{1-x}Ca_xCrO_3$ ($\sim$1.5 $Wm^{-1}\ K^{-1}$ at 500 K) [31] potentially highlights significant phonon scattering, the dominant phonon scattering mechanism(s) (boundary, magnon–phonon, short-range spin correlations, mass-disorder scattering, etc.) have yet to be identified.

Here, to disentangle the role of phonons and magnons, we present a detailed investigation of the lattice and spin dynamics, thermodynamics, and thermal transport of $YCrO_3$ using INS, Raman and IR spectroscopy ($5 \leqslant T \leqslant 300$ K and $0 \leqslant B \leqslant 5$ T), and C_p and κ measurements ($4 \leqslant T \leqslant 300$ K and $0 \leqslant B \leqslant 14$ T), combined with DFT simulations and phenomenological modeling. Using the combined set of techniques, and particularly the use of magnetic field application for spectroscopy, allows us to substantially clarify the relative contributions of different coupling mechanisms to the system thermodynamics.

2. Methods

2.1. Sample characterization

A polycrystalline sample of $YCrO_3$ was prepared by a solid-state reaction method [32]. Powder x-ray diffraction was recorded under ambient conditions using a Rigaku XRD instrument with Cu-Kα ($\lambda = 1.540\,60$ Å) source and D/tex ultra 1D detector in the $\theta/2\theta$ scanning mode. Data was collected from 20° to 80° in the 2θ scan range with scanning speed of 3° per minute. Crystal structure refinement was done using GSAS-I software [see supplementary figure 1 (https://stacks.iop.org/JPCM/00/000000/mmedia)]. The refined lattice parameters for an orthorhombic structure (*Pnma*, space group no. 62) are—$a = 5.5225(3)$ Å, $b = 7.5474(3)$ Å, $c = 5.2521(3)$ Å, $V = 218.914(12)$ Å^3. Lattice parameters obtained from the refinement are consistent with the previous x-ray and neutron diffraction studies [25, 27]. We note that our instrument resolution was inadequate to refine the structure in non-centrosymmetric phase (space group no. 4) as theoretically proposed in reference [19] below T_{FE}. The measured $T_N \sim 138$ K, determined from a peak in C_p measurements, is in good agreement with literature values [19, 23, 30] (see below).

2.2. Spectroscopy measurements

2.2.1. Inelastic neutron scattering measurements. Inelastic neutron scattering (INS) measurements on $YCrO_3$ were performed at the MARI time-of-flight chopper spectrometer at the ISIS Neutron and Muon Source in the UK The powder sample (mass ~ 10 g) was encased in a thin-walled aluminum can. We used a closed-cycle helium refrigerator for our measurements. Two incident neutron energies, $E_i = 35$ and 120 meV, were used at each temperature to probe magnetic excitations at low Q with high resolution and the full phonon spectra, respectively. The empty aluminum can was measured in identical conditions for all configurations. The Fermi chopper speed was kept at 400 and 300 Hz for $E_i = 120$ and 35 meV, respectively, thus providing an energy resolution (full width at half maximum) of ~3.8 and ~0.7 meV at the elastic line, which reduces to ~2.8 and ~0.4 meV at an energy transfer of 35 meV. The measured signal was transformed from instrument coordinates, scattering angle and neutron detection times, to the physical momentum transfer, Q, and energy transfer, E, using the MANTID software [33] to obtain the dynamical structure factor $S(Q, E)$. The dynamical susceptibility $\chi''(Q, E)$ were calculated from $S(Q, E)$ using $\chi''(Q, E) = (1 - \exp(-E/k_BT))S(Q, E)$. The phonon density of states (DOS) was obtained by integrating over $6 \leqslant Q \leqslant 10$ Å^{-1} (magnetic scattering was negligible beyond 6 Å^{-1}), and applying background and multi-phonon scattering corrections along with removal of the elastic peak as described in reference [34].

The phonon spectra from INS measurements are weighted by the relative neutron scattering strengths (σ/m) of the elements in the sample, where σ is the total neutron scattering cross-section, and m the atomic mass. The neutron weighting (NW) factors for Y, Cr, and O are $\sigma_Y/m_Y = 0.0866$, $\sigma_{Cr}/m_{Cr} = 0.0671$, and $\sigma_O/m_O = 0.2645$, respectively (in units of barns/amu). Consequently, the NW phonon DOS measured with INS, $g_{NW}(E)$, for $YCrO_3$ is over-weighted for the O vibrational contributions:

$$g_{NW}(E) = \frac{\left(\frac{\sigma_Y}{m_Y} g_Y(E) + \frac{\sigma_{Cr}}{m_{Cr}} g_{Cr}(E) + \frac{\sigma_O}{m_O} g_O(E)\right)}{\left(\frac{\sigma_Y}{m_Y} + \frac{\sigma_{Cr}}{m_{Cr}} + \frac{\sigma_O}{m_O}\right)} \quad (1)$$

where g_Y, g_{Cr}, and g_O are the partial DOS of Y, Cr, and O, respectively. The resulting NW phonon DOS is normalized to a unit area and can be directly compared against the simulated DOS to which the same neutron weights are applied.

2.2.2. Raman measurements. For Raman measurements, $YCrO_3$ powder was pelletized with polyvinyl alcohol (PVA) (organic binder). The pressed pellet was heated to 500 °C at the rate of 5 °C min^{-1}. After holding the temperature at 500 °C for four hours, it was further heated at the rate of 5 °C min^{-1} up to 1300 °C, and held for four hours. Cooling was done 5 °C min^{-1} down to 25 °C. T-dependent Raman measurements were performed in a backscattering geometry configuration using a Horiba Jobin-Yvon HR 800 Raman spectrometer equipped with a Peltier cooled charge-coupled device detector. A diffraction grating of 1800 groves/mm provided a spectral resolution of ~1 cm^{-1}. Raman measurements were done using a 632.8 nm He–Ne laser, which was focused on the sample using a 50X objective with the laser power of ~1 mW to avoid local heating. A liquid helium based closed-cycle cryostat along with LakeShore 335 temperature controller was used for T measurements from 300 K to 5 K (error of $\sim \pm 0.1$ K) in high vacuum of $\sim 10^{-6}$ mbar. Spectra were measured from 135–600 cm^{-1}. All spectra were fitted with a Lorentzian function to obtain phonon energies ω and linewidths Γ at full-width half maxima.

2.2.3. Infrared measurements. Far-infrared measurements were performed from 5 to 300 K on a powder sample of $YCrO_3$ dispersed in KBr matrix and in a magnetic field with field strength $B = 0$, 1 and 5 T in the spectral range 300–700 cm^{-1}. The sample was mounted on the sample insert of a cryogen free magneto-optical cryostat system (Spectromag-CFSM7T-1.5. Oxford Instruments, UK). Measurements were performed in transmission mode at a base pressure of $\sim 10^{-6}$ mbar with a resolution of 0.2 cm^{-1}. The measurement setup included a custom built Fourier transform spectrometer (Blue Sky Spectroscopy, Canada) with a Martin–Puplett interferometer

and wire grid polarizers, mercury arc lamp, and a cryogen free niobium transient edge sensor detector cooled down to 4 K. Background spectra were recorded in identical conditions. For B-dependent measurements, magnet was first ramped up to the required field, and then T was varied keeping magnet in persistent mode. The field direction at the sample position was horizontal along the direction of the IR beam.

2.3. Heat capacity and thermal conductivity measurements

A powder sample was mixed with PVA and pressed in a die to create a pellet with 15 mm diameter and ∼3–4 mm thickness. The pellet was sintered at 600 °C (ramped at the rate of 4 °C min^{-1}) for four hours. It was subsequently heated up to 1300 °C at the rate of 6 °C min^{-1}. Cooling was done at the rate of 4 °C min^{-1} down to 800 °C and at the rate of 6 °C min^{-1} from 800 °C to 25 °C.

C_p and κ measurements were performed using heat capacity (two-tau relaxation calorimetry) and thermal transport option of 14 T Dynacool PPMS (Quantum Design), respectively, in the range $4 \leqslant T \leqslant 300$ K and $0 \leqslant B \leqslant 14$ T. For C_p measurements, a flat and thin piece of mass ∼18.83 mg was cut from the sintered pellet and mounted on the calorimeter platform with Apiezon N grease. For κ measurements, a thin rod of ∼12 × 2× 2 mm was cut from the sintered pellet. Gold-coated copper leads (0.7 mm thick) were attached to the sample in four probe geometry with the help of two-component EPOTEK HE20 silver epoxy.

2.4. Simulations

2.4.1. Density functional theory simulations of phonons. Electronic structure simulations were performed in the framework of density functional theory (DFT) as implemented in the Vienna ab initio Simulation Package (VASP) [35–37]. We used 6 × 4 × 6Γ-centered Monkhorst-Pack electronic k-point mesh with the plane-wave cut-off energy of 520 eV on a 20 atom basis unit cell for the converged results. The convergence criteria for the self-consistent electronic loop was set to 10^{-8} eV. The projector-augmented-wave potentials explicitly included 11 valence electrons for Y ($4s^2 4p^6 5s^2 4d^1$), six for Cr ($3d^5 4s^1$), and six for O ($2s^2 2p^4$). We performed collinear spin-polarized calculations with the experimentally determined G-AFM order [27]. We used the generalized gradient approximation (GGA) in the Perdew–Burke–Ernzerhof parametrization [38] with a Hubbard correction. To treat the localized d-electron states of Cr in GGA + U calculations, we apply the method of Dudarev *et al* [39] with on-site Coulomb interaction $U = 3.7$ eV [40]. During structure relaxation, lattice parameters and atomic positions were optimized until forces on all atoms were smaller than 1 meV Å^{-1}. The resulting lattice parameters were—$a = 5.6178$ Å, $b = 7.6687$ Å, and $c = 5.3191$ Å, approximately 1.5% larger than the experimental lattice parameters at 300 K. Phonon dispersions were calculated in the harmonic approximation, using the finite displacement approach as implemented in Phonopy [41]. Atomic forces were obtained with VASP from 30 independent atomic displacements. The phonon calculations used a 2 × 2 × 2 supercell of the conventional cell containing 160 atoms. The atomic displacement amplitude was 0.01 Å. The simulated phonon DOS was red-shifted compared to the experimental phonon DOS at 5 K, and was multiplied by a factor of 1.1 for comparison. Grüneisen parameters were calculated for all phonon modes at the Γ point by applying 1% volumetric compression and expansion.

The same relaxed cell used for phonon calculations was used to estimate the Raman scattering intensity from density functional perturbation theory (DFPT) at the Γ point. The first derivative of the electric polarizability tensor, α_{mn}, was evaluated by displacing the atoms by mass-normalized phonon eigenvectors around minima in both directions and determining the change in the macroscopic dielectric tensor, ϵ. The remaining simulation details are described in reference [9]. Infrared activity is calculated using the Born effective-charge tensors and mass-normalized phonon eigenvectors following the implementation of Skelton *et al* [42].

2.4.2. Magnon simulations. To model the observed magnetic excitations, we calculated the magnon dispersions and powder average using linear spin wave theory as implemented in SpinW code [43] for the experimentally observed G-AFM order containing 4 Cr atoms per unit cell [27]. For SpinW calculations, we use the full moment. Powder averaging was performed with the parameter *nRand* set to 5000. We assumed nearest-neighbor (NN) interactions up to 5.52 Å. The first two NNs along in-plane and c-axis have distances of 3.77 and 3.81 Å, respectively, and are bridged by one anion. We follow the approximation of iso-structural $YFeO_3$ [44], and denote both interactions by J (see figure 1(c)). Similarly, the next three NNs bridged by two anions having distances of 5.25, 5.36, and 5.52 Å are represented by exchange constant J'. In our INS measurements, we did not observe any gap in the magnetic excitations at 5 K within our instrument resolution (∼0.7 meV). Thus, we do not include anisotropy terms in the spin Hamiltonian. Moreover, a recent neutron diffraction study has found the moments pointing along c-axis with zero canting (within the experimental resolution) in a–c and b–c planes [27], thereby making Dzyaloshinskii–Moriya interactions negligible. Even if we include canting in our simulations based on the presence of weak ferromagnetism in the magnetization measurements [19], a low energy magnetic excitation gap of the order of 100 μeV opens up, with little change to the remaining magnon dispersions or DOS. The fitted exchange constants are—$J = -2.7$ and $J' = -0.1$ meV (−ve sign is for the AFM interaction). We note that our results differ significantly from the exchange constants calculated in literature [20, 30] using Curie–Weiss and Néel temperature under mean-field theory ($J \sim -1.1$ to -1.7 meV, and $J' \sim -0.1$ to -0.4 meV). The simulated output, including the magnetic form factor of Cr^{+3} ($S = 3/2$), is shown in figure 3(c) illustrating an excellent agreement with INS measurements. The simulated magnon DOS was obtained by integrating over $0 \leqslant Q \leqslant 4$ Å^{-1} to powder average, but leaving out the magnetic form factor.

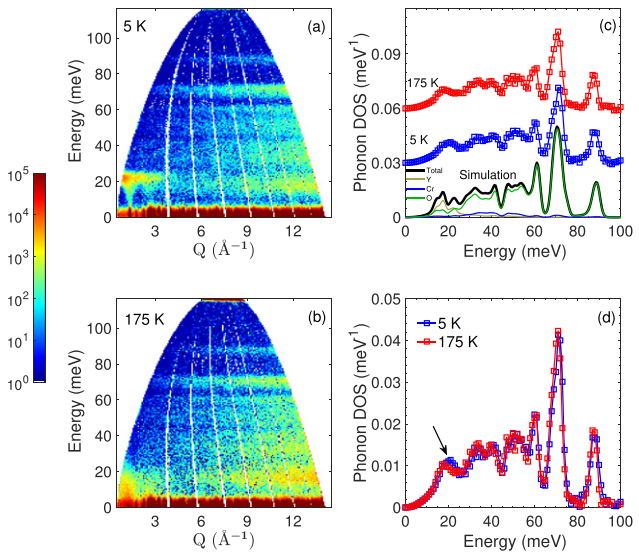

Figure 2. Phonons across T_N. (a) Dynamical structure factor $S(Q, E)$ of $YCrO_3$ measured using INS with $E_i = 120$ meV at 5 K showing the magnons (for $Q < 4$ Å^{-1}, and $E < 25$ meV) and phonons (for $Q > 4$ Å^{-1}, and $10 < E < 90$ meV). Well-defined phonon bands at constant energies are visible at high Q [see panel (c) for peak positions]. (b) Same as panel (a) but across T_N at 175 K. Intensity is in log scale and spans five decades. (c) Neutron-weighted phonon DOS of $YCrO_3$ measured using INS at 5 and 175 K compared with simulation results showing an excellent agreement throughout the energy range. Partial DOS of Y, Cr, and O atoms is also shown underneath the total DOS. Curves are offset. See details in the Methods section. (d) Same as panel (c) but experimental phonon DOS is over-plotted to highlight the difference near 20 meV across T_N (black arrow).

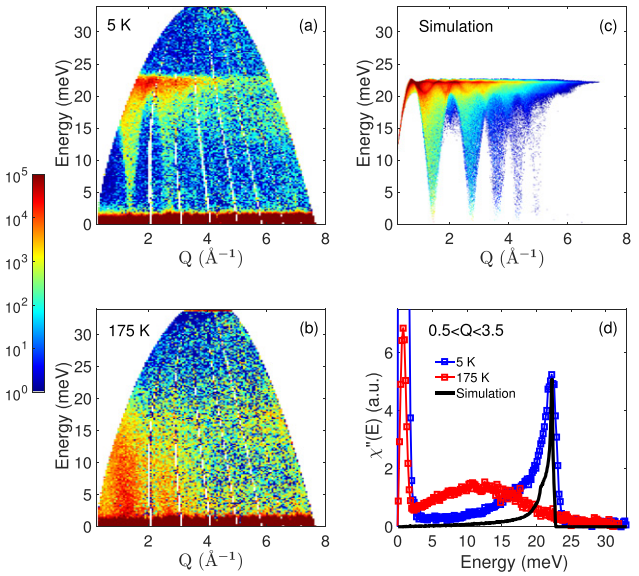

Figure 3. Magnetic excitations across T_N. (a) Dynamical structure factor $S(Q, E)$ of $YCrO_3$ measured using INS with $E_i = 35$ meV at 5 K showing high-resolution magnon spectra. Well-defined magnon dispersions emanating from magnetic Bragg peaks are visible below $Q < 3$ Å^{-1} that plateau near 22 meV. For $Q > 4$ Å^{-1}, intensity from phonons is also visible between 14 and 22 meV. (b) Same as panel (a) but across T_N at 175 K. The diffuse intensity is from the short-range spin correlations. Intensity is presented using a log scale and spans five decades. (c) Spin wave simulation of $YCrO_3$ including the magnetic form factor of Cr^{+3} ($S = 3/2$). (d) Integrated magnetic intensity $\chi''(E)$ ($0.5 < Q < 3.5$ Å^{-1}) from panel a-c after the Bose–Einstein occupation factor correction showing the evolution across T_N and comparison with simulation.

3. Results and discussion

3.1. Phonon dynamics

In the INS experiments, we measure the dynamical structure factor $S(Q, E)$, which includes the contribution from both phonons and magnons. The relative contribution of each quasiparticle type can be qualitatively separated by their momentum transfer (Q) dependence [45, 46]. The scattering intensity resultant from phonon contributions typically exhibits a Q^2 dependence. On the other hand, due to the finite size of the electron cloud, the magnetic form factor suppresses the magnetic intensity at large Q. Figure 2(a) shows the $S(Q, E)$ of $YCrO_3$ measured with incident neutron energy $E_i = 120$ meV at 5 K. One can see the magnons for $Q < 4$ Å^{-1} and $E < 25$ meV (discussed in section 3.2) and phonons for $Q > 4$ Å^{-1} and $10 < E < 90$ meV. On heating from 5 to 175 K, the scattering intensity increases due to an increase in the phonon occupation with temperature (see figure 2(b)). Following the procedure described in the Methods section, we calculated the NW phonon DOS from the measured $S(Q, E)$ at 5 and 175 K (figures 2(c) and (d)). The experimental NW phonon DOS is compared with simulated phonon DOS in figure 2(c) and shows excellent agreement. The partial phonon DOS of Y, Cr, and O are shown underneath the simulated curve highlighting significant contributions of O dominated modes above 35 meV, and mixed contribution of all atoms below 35 meV. We compare the experimental phonon DOS across T_N in figure 2(d) and observe little change except near 20 meV (marked by a black arrow). We confirmed that the change near 20 meV is from phonons and not from other sources, i.e., the sample can (aluminum has peak in the phonon DOS around 20 meV) or spin waves (peak in spin waves is around 22 meV as we discuss later). For confirmation, we carefully subtracted the sample background measured in identical conditions and obtained the phonons by exclusively taking data from high-Q, where the magnetic form factor reduces the magnetic intensity to less than 1%. The change in phonon DOS near 20 meV persisted. Near 20 meV, the phonon DOS has a large contribution from Y and O atoms. Hence this change originates from modulation of the force-constants between Cr–O and Cr–Y bonds due to change in the lattice potential as long-range order of Cr spins melts across T_N. We analyze the change in individual phonon modes across T_N in section 3.4.

3.2. Magnon dynamics

To model the magnons and determine the exchange constants, we carried out high-resolution INS measurements with $E_i = 35$ meV, which provided a resolution of ∼0.7 meV at the elastic line. The measured $S(Q, E)$ at 5 K is shown in figure 3(a). A well-defined magnon dispersions resultant from AFM ordered spins are seen emanating from the magnetic Bragg peaks at $Q \sim 1.4$ and ∼2.4 Å^{-1} which plateau at

$\sim$22 meV. Above T_N, magnetic Bragg peaks disappear due to loss of long-range spin correlations. However, short-range spin correlations persist. Such correlations are evident in our measurements at 175 K, which show a blob of intensity below 20 meV (see figure 3(b)). To understand the underlying mechanism of magnetic interactions, we model the magnons using linear spin-wave theory as implemented in SpinW code [43], as described in the Methods. The modeled magnon spectrum in figure 3(c) shows remarkable agreement with measurements at 5 K. We further compare the integrated magnetic intensity $\chi''(E)$ ($0.5 < Q < 3.5$ Å^{-1}) from panel (a)–(c) after correcting for Bose–Einstein occupation factor in panel (d). Again the peak at $\sim$22 meV is well reproduced. Our results reveal that NN interactions J between Cr ions bridged by one oxygen [i.e., Cr–O–Cr, see figure 1(a)] are quite strong ($J = -2.7$ meV), while the next nearest neighbor (NNN) interactions J' (Cr–O–O–Cr) are weak ($J' = -0.1$ meV). We note that Cr–O–Cr bonds of the CrO_6 polyhedron deviate slightly from the ideal superexchange interaction angle of 180° that promotes the AFM order [47]. The calculated exchange constants J and J' are of similar magnitude as obtained for the iso-structural $YFeO_3$ [44], where a similar mechanism of spins interaction was identified. However, our results differ significantly from the exchange constants calculated in literature using Curie–Weiss and Néel temperature under mean-field theory ($J \sim -1.1$ to -1.7 meV, and $J' \sim -0.1$ to -0.4 meV) [20, 30].

3.3. Thermodynamics of the magnetic phase transition

$YCrO_3$ is a wide-gap semiconductor with a bandgap of $\sim$1.8 eV [24]. Thus in the absence of electronic contributions, phonons and magnons can reliably describe the system thermodynamics. Given the excellent agreement between experiments and simulations, we can further reliably separate the individual contributions from phonons and magnons to the heat capacity (C_p) and entropy (S) to resolve the discrepancy surrounding the spin-reorientation transition. Previous analysis of C_p of $YCrO_3$ based on the Debye model suggested spin-reorientation [21, 23] but lacked experimental evidence in the magnetization measurements [22]. We note that fitting using the Debye model assumes that C_p is governed by phonons above T_N, which is not an appropriate assumption in the case of a strongly coupled system. In analogy with excess C_p of low-density glasses compared to their crystalline counterpart [48], the contribution of the paramagnetic state to C_p is not necessarily negligible. Moreover, as we saw earlier in INS measurements, short-range correlations persist above T_N. These correlations can also contribute significantly to C_p and entropy S. To be quantitative, in the paramagnetic state, the spin entropy is given by $k_B \ln(2J+1)$ [47, 49], where J is the sum of spin and orbital angular momentum. If we assume quenching of orbital momentum for Cr^{+3} (a reasonable assumption for 3d ions [47]), contribution from magnetic entropy S_{mag} is $1.39k_B$ per magnetic atom (or $\sim 0.3k_B$ atom^{-1}), which can no longer be neglected.

We have calculated the phonon contribution to heat capacity (C_{vib}) and entropy S_{vib} as follows,

$$C_{vib} = 3\int g(E)\, k_B \left(\frac{E}{k_B T}\right)^2 \frac{\exp(E/k_B T)}{(\exp(E/k_B T)-1)^2} \mathrm{dE}, \text{ and} \tag{2}$$

$$S_{vib} = 3Nk_B \int g(E)\,[(1+n_s)\ln(1+n_s) - n_T \ln(n_s)]\,\mathrm{d}E, \tag{3}$$

respectively [50, 51]. Here, $g(E)$ is the simulated phonon DOS at phonon energy E, k_B is Boltzmann's constant, $n_s(E) = [e^{E/k_B T} - 1]^{-1}$ is the Bose–Einstein occupation factor, and N is the number of atoms in the crystal. Since we have normalized $g(E)$ to an unit area, a factor 3 comes for three polarizations associated with phonons (two transverse and one longitudinal). We calculated $C_{vib}(T)$ and $S_{vib}(T)$ using the simulated phonon DOS, except for the change at the transition temperature (i.e., ΔC_{vib}^{138K} and ΔS_{vib}^{138K}), which was calculated using the measured NW phonon DOS at 5 and 175 K. C_{mag} and S_{mag} are obtained in a similar way, except that the pre-factor 3 is replaced by 1 (only one polarization for magnons [49]), and $g(E)$ replaced by the simulated magnon DOS (see Methods section for details). Thermal expansion also contributes to C_p and S (referred to as dilational contribution C_d and S_d) and is calculated as [51, 52],

$$C_d = \frac{\alpha(T)^2 V(T) T}{\chi(T)}, \text{ and} \tag{4}$$

$$S_d = \int_0^T \frac{\alpha(T')^2 V(T')}{\chi(T')} \mathrm{d}T'. \tag{5}$$

Here α is the volumetric thermal expansion coefficient, χ is the compressibility (inverse of bulk modulus), and V is the volume. For the calculation of C_d and S_d, we used $\alpha(T)$ and $V(T)$ from Udagawa *et al* [28] and χ from Su *et al* [53]. Moreover, the entropy can be calculated from experimental C_p data [51, 52],

$$S_{Exp.} = \int_0^T \frac{C_p(T')}{T'} \mathrm{d}T'. \tag{6}$$

Our calculations of C_p, C_{vib}, C_d, and C_{mag} are shown in figure 4. C_{vib} increases as a function of T and rises to more than $1k_B$ atom^{-1} near T_N. For C_{vib}, we find little change across T_N ($\Delta C_{vib}^{138K} \simeq 0.01 \pm 0.01 k_B$ atom^{-1}), thus indicating minimal role of magnon–phonon coupling in governing C_p. Moreover, C_{mag} is comparable in magnitude to C_{vib} and rises to $0.8k_B$ atom^{-1} near T_N. Because of the continuous evolution of the magnetic correlation length on heating above T_N, it is challenging to estimate the exact contribution; hence we limit our calculation of C_{mag} to below T_N. C_d shows a peak at T_N due to the discontinuity of α; however the contribution of this peak is an order of magnitude smaller than C_{vib} and C_{mag}. We compare the sum $C_{vib} + C_d + C_{mag}$ with C_p measurements at 0 T in figure 4(a). In general, agreement is quite good except for a small overestimation of 0.1 to $0.2k_B$ atom^{-1}, which could possibly arise from small difference in measured and calculated phonon DOS below 20 meV (see figure 2(c)) and/or from overestimation of C_d. We emphasize, since C_{vib} shows little change across T_N, the change in C_p near T_N ($\sim 0.15k_B$ atom^{-1}) originates from C_d ($0.03 \pm 0.01 k_B$ atom^{-1}) and the remaining contribution must arise from C_{mag} as the spin system long-range

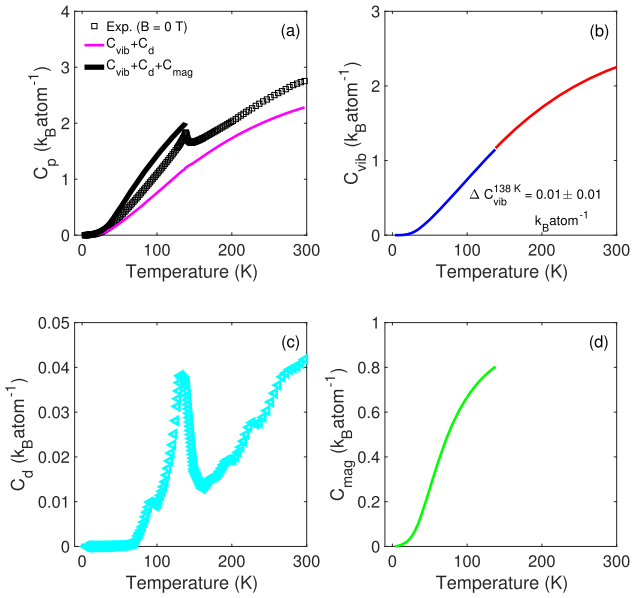

Figure 4. (a) A comparison of measured heat capacity C_p of $YCrO_3$ (black empty squares) at 0 T with sum contribution of vibrational ($C_{\rm vib}$), dilational ($C_{\rm d}$), and magnetic ($C_{\rm mag}$) contributions showing a good agreement. (b) $C_{\rm vib}$ as a function of temperature. Change in $C_{\rm vib}$ across $T_{\rm N}$ is $0.01 \pm 0.01 k_{\rm B}$ atom^{-1}, as determined from change in the experimental phonon DOS. (c), (d) $C_{\rm d}$ and $C_{\rm mag}$ as a function of temperature. The peak in $C_{\rm d}$ is due to the sudden change in thermal expansion near $T_{\rm N}$. $C_{\rm mag}$ is calculated below $T_{\rm N}$ from the simulated magnon DOS. Calculation details are provided in the text.

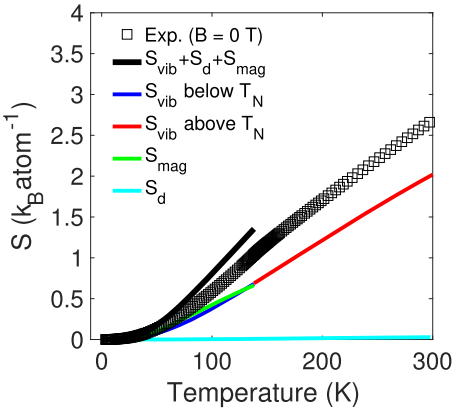

Figure 5. Contributions to the total entropy S of $YCrO_3$. Vibrational, dilational, and magnetic entropy are denoted by $S_{\rm vib}$, $S_{\rm d}$, and $S_{\rm mag}$, respectively. Below $T_{\rm N}$, $S_{\rm vib}$ and $S_{\rm mag}$ are comparable. The change in $S_{\rm vib}$ across $T_{\rm N}$ is $0.01 \pm 0.01 k_{\rm B}$ atom^{-1}, as determined from change in the experimental phonon DOS. Experimental entropy markers are obtained from C_p measurements. Calculation details are provided in the text.

correlations are lost. Furthermore, we note that our measurements or simulations show no evidence of spin-reorientation or a maximum in $C_{\rm mag}$ near 60 K as suggested in references [21, 23], consistent with the magnetization study of Dasari *et al* [22]. Our C_p measurements conducted in magnetic fields up to $B = 14$ T also did not show any indication of structural or magnetic phase transitions (see supplementary figure 8). However, on increasing B from 0 to 14 T, $T_{\rm N}$ increases by $\sim$3 K and the peak in C_p is gradually broadened.

Our analysis of S separating the contributions from $S_{\rm vib}$, $S_{\rm mag}$, and $S_{\rm d}$ along with experimental data at 0 T is shown in figure 5. As one can see, while $S_{\rm d}$ is quite small up to 300 K, $S_{\rm vib}$ and $S_{\rm mag}$ have comparable contributions below $T_{\rm N}$. Similar to $C_{\rm vib}$, the change in $S_{\rm vib}$ is negligible ($\Delta S_{\rm vib}^{138\rm K} \simeq 0.01 \pm 0.01 k_{\rm B}$ atom^{-1}) across $T_{\rm N}$. A comparison of the sum $S_{\rm vib} + S_{\rm d} + S_{\rm mag}$ with experimental values of S shows good agreement. An overestimation of 0.1 to $0.2 k_{\rm B}$ atom^{-1} can be rationalized following similar reasoning discussed for C_p.

3.4. Phonon scattering mechanism across the magnetic phase transition

While INS measurements provide an excellent description of phonons over the entire Brillouin zone, the lack of instrument resolution makes it challenging to precisely estimate changes in phonon energies (ω) and linewidths (Γ, full width at half maximum) across $T_{\rm N}$, expected to be of the order of $\sim$1 meV ($\simeq$8 cm^{-1}). Raman and IR spectroscopy can measure phonons with a resolution exceeding 1 cm^{-1}. From symmetry analysis of $YCrO_3$, there are 24 Raman active modes [$7A_g + 5B_{1g} + 7B_{2g} + 5B_{3g}$] and 25 IR active modes [$9B_{1u} + 7B_{2u} + 9B_{3u}$]. Our intensity simulations of Raman and IR active modes using DFPT identify all the active modes (some modes are extremely weak) and are shown in supplementary figure 3.

Supplementary figure 2 shows Raman and IR measurements in a broad temperature range of 5 to 300 K. In these measurements, we observe 15 Raman active and 12 IR active modes that are visible in our simulations with reasonably strong intensity. We note that IR spectra are only analyzed above 375 cm^{-1} because of the strong absorption of KBr. We assign the symmetry of observed modes based on our Raman intensity simulations and display them underneath the respective peaks. The symmetry assignment is consistent with previous Raman measurements in literature [28–30, 54]. Although our simulations predict intensities reasonably well for most Raman active modes, glaring discrepancies exists for $B_{2g}(3)$, $B_{3g}(2)$, $A_g(4)$, $B_{2g}(6)$, and $B_{2g}(7)$ symmetry modes. The discrepancy is apparent because the macroscopic dielectric constant (ϵ) is calculated by freezing the phonon mode eigenvectors with fixed magnetic moment obtained from an undistorted unit cell, which does not accurately account for changes in the electron screening. This simplification induces error in ϵ and consequently, in the Raman polarizability tensor. However, our intensity simulations of IR active peaks, which do not require the calculation of ϵ for each phonon eigenvectors, are in close agreement with measured data. We rely on our simulations to assign symmetries of the IR active modes.

We subsequently fitted all Raman and IR active peaks to extract ω and Γ, and show the results in supplementary table 1 along with ω obtained from DFT simulations and previous measurements [54]. We present ω and Γ of six selected modes with different symmetry in figure 6 and compare with quasi-harmonic simulations [51] by integrating $\frac{\partial \omega}{\omega} = -\gamma \frac{\partial V}{V}$. The remaining modes are shown in supplementary figure 4. Here V is the volume, and γ is the Grüneisen parameter obtained from DFT simulations as described in the Methods section. We note that our data, consistent with previous Raman measurements

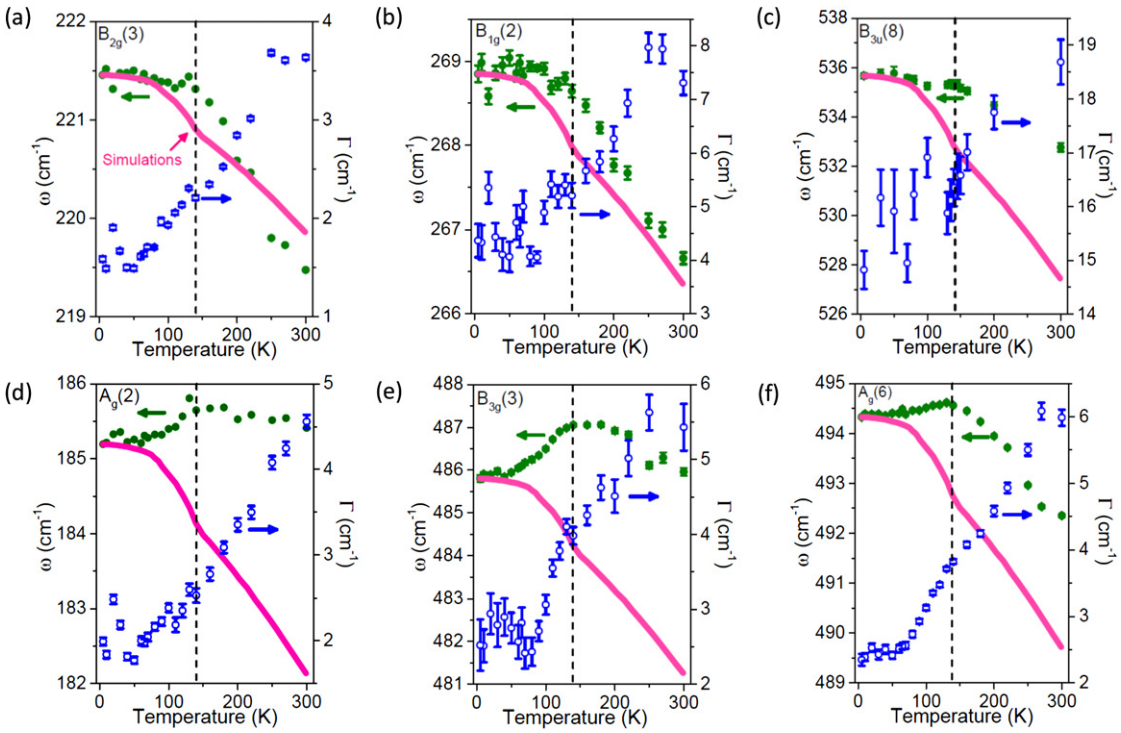

Figure 6. (a) Phonon energy, ω, of $B_{2g}(3)$ symmetry mode (filled green circles and left axis) as a function of T. Black dashed vertical line is at $T = T_N$. Experimental values are compared with ω obtained from DFT simulations under quasi-harmonic approximation (magenta line). See details in the text. Phonon linewidth at full width half maximum, Γ, (empty blue circles) as a function of T are shown on the right axis. (b)–(e) Same as panel (a) but for (b) $B_{1g}(2)$, (c) $B_{3u}(8)$, (d) $A_g(2)$, (e) $B_{3g}(3)$, and (f) $A_g(6)$ symmetry modes. Error bars denote one standard deviation.

[28, 29], do not show any anomaly near ∼60 K, proposed to arise from spin-reorientation in reference [30]. As we can see from figures 6(a) and (b), experimental and simulated ω of $B_{2g}(3)$ and $B_{1g}(2)$ symmetry modes agree well. $B_{3u}(8)$ symmetry mode shows a weaker T-dependence than simulations but follows the experimental trend (see figure 6(c)). However, as seen from figures 6(d)–(f), ω of $A_g(2)$, $B_{3g}(3)$, and $A_g(6)$ symmetry modes deviate strongly from the measurements, and their T-dependence below T_N is opposite the prediction from the simulations. This anomalous T-dependence of some A_g and B_{1g} symmetry modes is also seen in reference [29]. If this unusual behavior originates from magnon–phonon coupling, we should see an abrupt drop or a decrease in Γ on heating above T_N as magnon–phonon scattering channels disappear due to loss of long-range spin coherence. However, all modes show a monotonic rise of Γ with a little or no change across T_N.

We further performed IR measurements up to 5 T to alter the magnon–phonon coupling by modifying the lattice Hamiltonian [17, 18], and induce magnetostriction effects [11] (lattice strains will scatter phonons and increase Γ). Our measurements showed no observable change within the error bars of ω or Γ (see figure 7). Hence, we can safely exclude the role of magnon–phonon coupling and magnetostriction effects (also confirmed by κ measurements and simulations, see section 3.5). We mention here that phonon measurements under magnetic field are quite limited in the literature (up

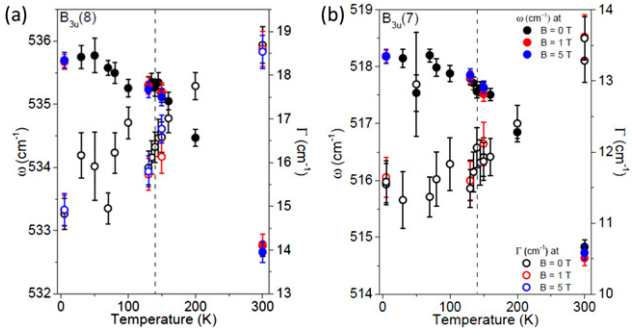

Figure 7. (a) Phonon energy ω (filled markers), and linewidth Γ (empty markers), of $B_{3u}(8)$ symmetry mode as a function of T for applied magnetic fields of $B = 0$ (black circles), 1 (red circles), and 5 T (blue circles). $B_{3u}(8)$ symmetry mode is also shown in figure 6(c). (b) Same as panel (a) but for $B_{3u}(7)$ symmetry mode. Error bars denote one standard deviation.

to 100 cm^{-1} is accessible via THz spectroscopy). A dedicated IR free-electron laser facility allowed us to probe ω up to 650 cm^{-1} with an unprecedented spectralresolution of 0.2 cm^{-1}. We carefully analyzed the eigenvectors of all symmetry modes (see supplementary figure 7), and find that modes with different eigenvectors show this unusual T-dependence, with no unique pattern discernible from the atomic displacement patterns. For example—the $A_g(2)$ mode has CrO_6 polyhedron tilt about the a-axis and rotation about the b-axis, $B_{3g}(3)$ is a Jahn–Teller distortion, and $A_g(6)$ is tilt about the

a-axis. Thus, we cannot single-out certain symmetry modes or patterns that respond anomalously. The remaining possibility of the observed behavior is magnetoelastic effects. As the lattice contracts anisotropically below T_N [28, 32], the changing lattice potential results in phonon softening on cooling below T_N for certain phonon modes. Importantly, magnetoelastic effects do not scatter phonons [12, 29] as the resulting phonon softening is generally small and does not alter the scattering phase space across T_N as confirmed by our experiments. In conclusion, our T- and B-dependent ω and Γ measurements allow us to attribute the observed behavior to magnetoelastic effects and exclude the role of magnon–phonon, and magnetostriction effects. Our κ measurements and simulations further support the same conclusion, as we demonstrate in the next section 3.5.

3.5. Thermal transport and phonon scattering mechanism

κ in magnetic semiconductors and insulators often show significant suppression and nearly constant T-dependence above T_N, resulting directly from the dominant contributions of phonons to this term. This unusual behavior is analyzed in detail for $YMnO_3$ [55], $CuCrO_2$ [12], and CrN [56], and was reported to result from non-adiabatic effects arising from dynamic coupling between short-range spin correlations and phonons. The dynamic coupling significantly suppresses the phonon lifetimes, hence suppressing the κ above T_N. Because of low κ of $YCrO_3$ ($\sim$1.2 Wm^{-1} K^{-1} at 200 K and 0 T, measured in this work), we examined whether similar dynamic coupling could be the dominant phonon scattering mechanism here.

In general, phonons can be scattered by point-defects, boundaries, other phonons (Umklapp scattering), electrons, and magnons. Since $YCrO_3$ is a wide-gap semiconductor (E_g is $\sim$1.8 eV [24]), we neglect electron–phonon coupling. If we assume all scattering processes to be independent of each other, following Matthiessen's rule, the total phonon scattering rate of τ^{-1} is given as,

$$\tau^{-1} = \tau_{PD}^{-1} + \tau_{B}^{-1} + \tau_{U}^{-1} + \tau_{SF}^{-1}. \quad (7)$$

where τ_{PD}^{-1}, τ_{B}^{-1}, τ_{U}^{-1}, and τ_{SF}^{-1} denote point-defects, boundary, Umklapp, and short-range spin correlation scattering processes. We note that scattering from short-range spin correlations is only included above T_N. The scattering rates from these scattering mechanisms can be modeled as [57, 58],

$$\tau^{-1} = V\frac{\omega^4}{4\pi v_g^3}\left(\frac{\Delta M}{M}\right)^2 + \frac{v_g}{L} + P\frac{\hbar\gamma^2}{M v_g^2 \theta_D}\omega^2 T^n \exp\left(-\frac{\theta_D}{mT}\right) + C_{SF} v_g. \quad (8)$$

Here, V is the volume per unit cell, v_g and ω are the phonon group velocity and phonon frequency, $\Delta M/M$ is the point-defect ratio, L is the particle/grain size, θ_D is the Debye temperature, γ is an average Grüneisen parameter, P, n, and m are Umklapp scattering parameters of order one, C_{SF} is the proportionality constant for phonon scattering from spin-fluctuations and is given by $\rho_0\pi(\xi/2)^2$. ρ_0 is the density of scatterers, and ξ is correlation length proportional to the strain fields generated by spin-fluctuations [55]. For analysis, we consider C_{SF} as a free parameter under the constraint (required for self-consistency) that the average distance, $d = 2(3/4\pi\rho_0)^{1/3}$, between two scatterers, will be greater than ξ [12, 55]. Aside from mass disorder from besides from impurities and oxygen vacancies, point-defect scattering can also arise from perturbations in force-constants and nearest-neighbor distances. However, since their effects are expected to be small [12], we exclude them from our analysis. We estimate the mass-disorder and boundary scattering by fitting the κ at low-T ($T < 20$ K), and find $\Delta M/M = 0.066$, and L (i.e., particle size) of the order of $\sim$55 nm. The calculated particle size is consistent with scanning electron microscope micrographs, where particles ranging from 50 to 1000 nm are visible [24]. From the first moment of the phonon DOS, θ_D is calculated to be 733 K ($\theta_D = \frac{4\langle E\rangle}{3k_B}$, where $\langle E\rangle = \int g(E)E\mathrm{d}E$) [12]. Umklapp scattering parameters, n and m are kept constant at 1.0, and $\sim 2N^{1/3} = 5.43$, respectively [12]. We calculated average $\gamma = 1.66$ from DFT simulations and is similar to the value reported elsewhere [25]. Since our simulation results show excellent agreement with the measured phonons, q-dependent phonon energy and group velocity are also obtained from DFT simulations.

The effect of various scattering mechanisms on κ along with modeling is shown in figure 8(a). Individual curves show the κ values if all other scattering mechanisms were absent. As one can observe, at low-T, mass-disorder and boundary scattering are the dominant mechanisms. Conversely, due to increased phonon occupation on heating, Umklapp scattering becomes the dominant scattering mechanism above 100 K. Since the measured κ decreases linearly with T, conventional wisdom dictates that Umklapp scattering must remain the dominant mechanism at high-T. Indeed our analysis suggests that above T_N phonon scattering from short-range spin correlations is considerably weaker than Umklapp scattering, which is consistent with a continuous rather than an abrupt increase of Γ across T_N as seen in ours (see figure 6) and in a previous study [29]. This observed behavior is similar to the dominant scattering mechanism in non-magnetic semiconductors and insulators. However, it is in contrast to the prevalent scattering mechanism observed in magnetic semiconductors and insulators, as described earlier. In regards to the low value of κ, we should mention that κ in polycrystalline samples is strongly dependent on particle/grain size. For example, for the same level of mass-disorder, a single-crystal with a minimum boundary length of 1 mm will have $\kappa \sim 15$ Wm^{-1} K^{-1} at 100 K because of suppression of the boundary scattering. This substantial increase in single-crystals is not unexpected and has been observed in $YMnO_3$, where κ in the single-crystal sample increased to $\sim$10 Wm^{-1} K^{-1} from the polycrystalline value of $\sim$1 Wm^{-1} K^{-1} at 50 K (see figures 1 and 4 of reference [55]).

The κ along three crystallographic directions are shown in figure 8(b). As one can see, κ is maximum along the c-axis and minimum along the a-axis. This anisotropy in our simulated κ can be rationalized based on the phonon group velocities, v_g. As shown in supplementary table 2, while the v_g of transverse acoustic modes is

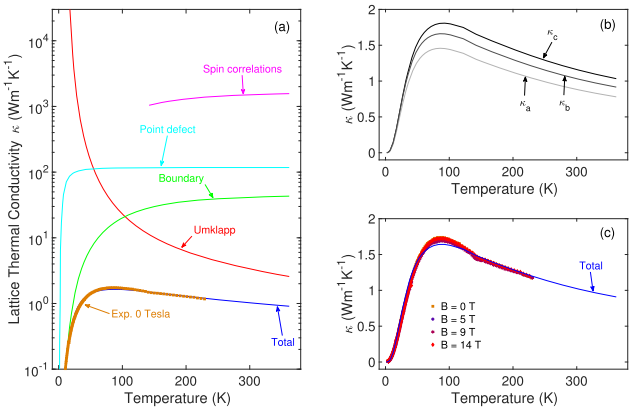

Figure 8. (a) The lattice thermal conductivity κ of $YCrO_3$ due to various scattering mechanisms compared with measured κ in a polycrystalline sample at 0 T. Individual curves show κ values if all other scattering mechanisms were absent. (b) Calculated κ along three crystallographic directions showing anisotropy owing to different phonon group velocity. (c) Measured κ for different values of an applied magnetic field, B. We note that for the same level of mass-disorder, a single-crystal having a minimum dimension of 1 mm will have $\kappa \sim 15$ Wm^{-1} K^{-1} at 100 K. See discussion in the text.

comparable along the three directions, longitudinal acoustic modes show large variation with maximum value along the c-axis (9291 ms^{-1}) in comparison to 6604 ms^{-1} along the a-axis. We note we have assumed all scattering mechanisms to be isotropic; however, if τ^{-1} is anisotropic, the general trend may change.

Thus far, we have excluded the contribution of magnons to the κ below T_N, which may not be negligible. In experiments, we measure the total κ which includes the contribution from both phonons and magnons. Since our measured κ showed little change across T_N [only a small kink is visible in figure 8(c)], it suggests a relatively small contribution of magnons to κ, consistent with approximation made in other magnetic semiconductors [55] and justifying our exclusion of magnons in the modeling of κ. We further assess the role of magnon–phonon coupling and magnetostriction effects by measurement of κ up to $B = 14$ T as shown in figure 8(c). Holz *et al* [17] had shown that at large B, the lattice Hamiltonian is modified, implying magnon–phonon coupling will be altered too. Moreover, lattice strains due to magnetostriction effects at large B will scatter phonons and decrease the κ. Our measurements as a function of B remain essentially the same (within the error bars of measurements, which is $\sim$10% of the measured value), thus excluding any significant role of magnon–phonon coupling and magnetostriction effects on κ. Their minimal role is also evident from Γ values extracted in section 3.4, which showed a monotonic response of Γ as a function of T. Here we mention that phonon scattering due to magnon–phonon coupling (not included in our model for reasons discussed above) is different from phonon scattering by short-range spin correlations (explicitly included in our model). While magnon–phonon coupling scatters phonon below T_N, phonon scattering from short-range spin correlations is above T_N. As we have shown by detailed analysis, both scattering mechanisms have minimal effect on κ of $YCrO_3$.

4. Conclusions

We investigated the T- and B-dependence of lattice and spin dynamics, thermodynamics, and thermal transport by combining experiments and first-principles simulations. Our INS, and Raman and IR spectroscopy results as a function of T and B reveal little change of phonon energies (ω) and linewidths (Γ) across T_N suggesting a minimal role of magnon–phonon coupling, spin-fluctuations, and magnetostriction effects on the lattice response. Softening of ω for specific modes on cooling below T_N was rationalized based on magnetoelastic coupling. Our magnon modeling using linear spin-wave theory finds NN superexchange interactions (Cr–O–Cr) to be quite strong compared to the NNN interactions (Cr–O–O–Cr). Thermodynamic modeling using INS data on phonons and magnons show a significant contribution of spins to C_p and S. However, we did not find an anomaly in the C_{mag} at $\sim$60 K, which was proposed to arise from a spin-reorientation transition. Our κ measurements and phenomenological modeling, consistent with spectroscopy results, confirm a minimal role for spins in phonon scattering, but show substantial scattering from boundaries and three-phonon processes. Our results highlight the need for combined spectroscopy, thermodynamics, and thermal transport measurements along with simulations to quantify and delineate the role of various quasi-particle interactions and scattering on phonons and their corresponding role in thermal transport.

Acknowledgments

APR acknowledges the financial support from IRCC-IITB. NB and DB thanks the financial support from BRNS-DAE under the Project No. 58/14/30/2019-BRNS/11117, and MHRD-STARS under the Project No. STARS/APR2019/PS/345/FS. The simulations were performed at the ~~ANUPAM super-computing facility at BARC and~~ SPACETIME super-computing facility at IITB. Experiments at the ISIS Neutron and Muon Source were supported by a beamtime allocation RB1990348 from the Science and Technology Facilities Council. Authors thank the Department of Science and Technology, India (SR/NM/Z-07/2015) for the access to the experimental facility and financial support to carryout the experiment, and Jawaharlal Nehru Centre for Advanced Scientific Research (JNCASR) for managing the project. UGC-DAE CSR, Indore is acknowledged for extending their Raman spectroscopy facilit

ORCID iDs

J L Niedziela https://orcid.org/0000-0002-2990-923X
Dipanshu Bansal https://orcid.org/0000-0003-1181-1119

References

[1] Norman M 2014 *Novel Superfluids* ed K H Bennemann and J B Ketterson vol 2 (Oxford: Oxford University Press) Chap. Unconventional Superconductivity

[2] Stewart G R 2017 *Adv. Phys.* **66** 75
[3] Imada M, Fujimori A and Tokura Y 1998 *Rev. Mod. Phys.* **70** 1039
[4] Fiebig M, Lottermoder T, Meier D and Trassin M 2016 *Nat. Rev. Mater.* **1** 16046
[5] Budai J D *et al* 2014 *Nature* **515** 535
[6] Bansal D *et al* 2020 *Nat. Phys.* **16** 669
[7] Young J, Stroppa A, Picozzi S and Rondinelli J M 2015 *J. Phys.: Condens. Matter* **27** 283202
[8] Bansal D, Niedziela J, Sinclair R, Garlea V, Abernathy D, Chi S, Ren Y, Zhou H and Delaire O 2018 *Nat. Commun.* **9** 15
[9] Bansal D *et al* 2019 *Phys. Rev.* B **100** 214304
[10] Lee S *et al* 2008 *Nature* **451** 805
[11] Kimura K, Otani T, Nakamura H, Wakabayashi Y and Kimura T 2009 *J. Phys. Soc. Japan* **78** 113710
[12] Bansal D *et al* 2017 *Phys. Rev.* B **95** 054306
[13] Pimenov A, Mukhin A A, Ivanov V Y, Travkin V D, Balbashov A M and Loidl A 2006 *Nat. Phys.* **2** 97
[14] Petit S, Moussa F, Hennion M, Pailhés S, Pinsard-Gaudart L and Ivanov A 2007 *Phys. Rev. Lett.* **99** 266604
[15] Toth S *et al* 2016 arXiv:1606.07321
[16] Wu X, Liu Z and Luo T 2018 *J. Appl. Phys.* **123** 085109
[17] Holz A 1972 *Nuovo Cimento* B **9** 83
[18] Jin H, Restrepo O D, Antolin N, Boona S R, Windl W, Myers R C and Heremans J P 2015 *Nat. Mater.* **14** 601
[19] Serrao C R, Kundu A K, Krupanidhi S, Waghmare U V and Rao C 2005 *Phys. Rev.* B **72** 220101
[20] Tsushima K, Aoyagi K and Sugano S 1970 *J. Appl. Phys.* **41** 1238
[21] Durán A, Arévalo-López A M, Castillo-Martínez E, García-Guaderrama M, Moran E, Cruz M P, Fernández F and Alario-Franco M A 2010 *J. Solid State Chem.* **183** 1863
[22] Dasari N, Mandal P, Sundaresan A and Vidhyadhiraja N S 2012 *Europhys. Lett.* **99** 17008
[23] Durán A, Escamilla R, Escudero R, Morales F and Verdín E 2018 *Phys. Rev. Mater.* **2** 014409
[24] Tiwari S, Saleem M, Mishra A and Varshney D 2019 *J. Supercond. Novel Magn.* **32** 2521
[25] Zhu Y *et al* 2020 *Phys. Rev.* B **101** 014114
[26] Lilienblum M, Lottermoser T, Manz S, Selbach S M, Cano A and Fiebig M 2015 *Nat. Phys.* **11** 1070
[27] Salazar-Rodriguez R, Aliaga-Guerra D and Taddei K M 2019 *Hyperfine Interact.* **240** 82
[28] Udagawa M, Kohn K, Koshizuka N, Tsushima T and Tsushima K 1975 *Solid State Commun.* **16** 779
[29] Bhadram V S, Rajeswaran B, Sundaresan A and Narayana C 2013 *Europhys. Lett.* **101** 17008
[30] Sharma Y, Sahoo S, Perez W, Mukherjee S, Gupta R, Garg A, Chatterjee R and Katiyar R S 2014 *J. Appl. Phys.* **115** 183907
[31] Weber W J, Griffin C W and Bates J L 1987 *J. Am. Ceram. Soc.* **70** 265
[32] Gupta M K, Mittal R, Mishra S K, Goel P, Singh B, Rols S and Chaplot S L 2020 arXiv:2004.01731
[33] Arnold O *et al* 2014 *Nucl. Instrum. Methods Phys. Res. Sect.* A **764** 156
[34] Bansal D, Li C, Said A, Abernathy D, Yan J-Q and Delaire O 2015 *Phys. Rev.* B **92** 214301
[35] Kresse G and Hafner J 1993 *Phys. Rev.* B **47** 558
[36] Kresse G and Furthmüller J 1996 *Phys. Rev.* B **54** 11169
[37] Kresse G and Furthmüller J 1996 *Comput. Mater. Sci.* **6** 15
[38] Perdew J P, Burke K and Ernzerhof M 1996 *Phys. Rev. Lett.* **77** 3865
[39] Dudarev S L, Botton G A, Savrasov S Y, Humphreys C J and Sutton A P 1998 *Phys. Rev.* B **57** 1505
[40] Persson K Materials data on $YCrO_3$ (SG:62) by Materials Project. **Q7**
[41] Togo A and Tanaka I 2015 *Scr. Mater.* **108** 1
[42] Skelton J M, Burton L A, Jackson A J, Oba F, Parker S C and Walsh A 2017 *Phys. Chem. Chem. Phys.* **19** 12452
[43] Toth S and Lake B 2015 *J. Phys.: Condens. Matter* **27** 166002
[44] Amelin K, Nagel U, Fishman R S, Yoshida Y, Sim H, Park K, Park J-G and Rõõm T 2018 *Phys. Rev.* B **98** 174417
[45] Squires G 1978 *Introduction to the Theory of Thermal Neutron Scattering* (Cambridge: Cambridge University Press)
[46] Willis B and Carlile C 2009 *Experimental Neutron Scattering* (Oxford: Oxford University Press)
[47] Blundell S 2001 *Magnetism in Condensed Matter* (New York: Oxford University Press)
[48] Chumakov A I *et al* 2014 *Phys. Rev. Lett.* **112** 025502
[49] Grimvall G 1999 *Thermophysical Properties of Materials* (Amsterdam: Elsevier)
[50] Wallace D 1972 *Thermodynamics of Crystals* (New York: Wiley)
[51] Fultz B 2010 *Prog. Mater. Sci.* **55** 247
[52] Bansal D, Hong J, Li C, May A, Porter W, Hu M, Abernathy D and Delaire O 2016 *Phys. Rev.* B **94** 054307
[53] Su Y, Guo J, Cheng X, Feng S and Yang Y 2019 *J. Alloys Compd.* **805** 489
[54] Todorov N, Abrashev M, Ivanov V, Tsutsumanova G, Marinova V, Wang Y-Q and Iliev M 2011 *Phys. Rev.* B **83** 224303
[55] Sharma P, Ahn J, Hur N, Park S, Kim S, Lee S, Park J-G, Guha S and Cheong S-W 2004 *Phys. Rev. Lett.* **93** 177202
[56] Stockem I, Bergman A, Glensk A, Hickel T, Körmann F, Grabowski B, Neugebauer J and Alling B 2018 *Phys. Rev. Lett.* **121** 125902
[57] Klemens P 1958 *Solid State Physics* (*Advances in Research and Applications-Thermal Conductivity and Lattice Vibrational Modes*) vol 7 (New York: Academic)
[58] Tritt T 2004 *Thermal Conductivity* (*Theory, Properties, and Applications*) (New York: Kluwer Academic/Plenum Publishers)